

Giant Radio Sources as a probe of the cosmological evolution of the IGM, II. The observational constraint for the model of the radio-jets propagation through the X-ray halo–IGM interface

E. Kuligowska, M. Jamrozy, D. Koziel-Wierzbowska, and J. Machalski

Astronomical Observatory, Jagiellonian University, ul. Orła 171, 30-244, Kraków, Poland
e-mail:(elzbieta,jamrozy,eddie,machalsk)@oa.uj.edu.pl

Received October 9, 2009

ABSTRACT

Three limited samples of high-redshift radio sources of FR II-type are used to constrain the dynamical model for the jets' propagation through the two-media environment: the X-ray emitting halo with the power-law density profile surrounding the parent galaxy and the much hotter intergalactic medium (IGM) of a constant density. The model originally developed by Gopal-Krishna & Wiita (1987) is modified adopting modern values of its free parameters taken from recent X-ray measurements with the XMM-Newton and Chandra Observatories. We find that (i) giant-sized radio sources (~ 1 Mpc) exist at redshifts up to $z \sim 2$, (ii) all newly identified the largest radio sources with $1 < z < 2$ appeared to be quasars, (iii) all of them are younger and expanding faster than their counterparts at lower redshifts, and (iv) the above properties are rather due to the powerful jets than peculiar environmental conditions (e.g. voids) in the IGM. The extreme powerful jets may testify to a dominant role of the accretion processes onto black holes in earlier cosmological epochs.

Key words: *Galaxies: active – Galaxies: evolution – intergalactic medium*

1. Introduction

In Paper I of this series (Machalski, Koziel-Wierzbowska & Jamrozy, 2007) a problem of the cosmological evolution of the intergalactic medium (IGM) was recalled and a necessity to find distant ($z > 0.5$) "giant"-sized radio sources (hereafter referred to as GRSs) with a very low energy densities in their extended lobes, to solve this problem, was emphasised. Extended large-sized double radio sources are not easy to recognise because of their relatively low radio brightness and a difficulty to detect eventual bridge connecting brighter parts (lobes) of a common radio structure. Several observational efforts show that most of known GRSs lie at low redshifts of $z < 0.25$. For a long time this caused a presumption that such extragalactic double radio sources, especially those of FR II-type, did not exist at redshifts higher than about 1 because of the expected strong evolution of a uniform IGM, $\rho_{\text{IGM}} \propto (1+z)^3$, confining the lobes of sources (e.g. Kapahi 1989). The

situation changed over 10 years ago when Cotter, Rawlings & Saunders (1996) and Cotter (1998) presented an unbiased sample of giant radio sources selected from the 7C survey (McGilchrist et al. 1990). Their sample comprised 12 large-size sources with $0.3 < z < 0.9$; four of them having $D > 1$ Mpc have been included in Table 1 of Paper I, where there was shown that a list of known GRSs with $z > 0.5$ and $D > 1$ Mpc is very short.

The undertaken search for such GRSs on the southern sky hemisphere with the 11m SALT telescope during the Performance Verification (P–V) phase has resulted in the detection of 21 GRSs with the projected linear size greater than 1 Mpc. However, we found that their redshifts do not exceed the value of 0.4 and the energy density in only two of them is less than 10^{-14} J/m³. We serendipitously discovered that one of them (J1420–0545) is, in fact, the largest GRS in the Universe (cf. Machalski et al. 2008).

Dynamical considerations relating to propagation of a bow shock at the head of powerful supersonic jet through the galactic and/or intergalactic medium (e.g. Arnaud et al. 1984; Begelman & Cioffi 1989; Falle 1991) predict that the lengthening of a channel along which the jet flows is governed by the balance between the jet's thrust and the ram pressure of the ambient medium. This balance implies that if the channel elongates at a rate faster than the rate at which the jet delivers energy, the motion of the jet's head would slow down until it become subsonic. This should cause a drastic reduction in both the speed and radiation of the head, thus effectively limiting further growth of the radio structure both in size and luminosity. Such a scenario is incorporated in the analytical model for the evolution of FR II-type radio sources of Kaiser, Dennett-Thorpe & Alexander (1997; hereafter referred to as KDA) which combines the dynamical model of Kaiser & Alexander (1997) with the model for expected radio emission under the influence of energy loss processes.

The dynamical evolution of a FR II radio source strongly depends on characteristics of the ambient medium. Gopal-Krishna & Wiita (1987) proposed the two-medium model consisting of an X-ray halo around the parent galaxy with gas density decreasing with radial distance from the galaxy and a much hotter intergalactic medium (IGM) with constant density. These two media were conceived to be pressure-matched at their interface. It is worth noting that their model (hereafter referred to as G-KW model) does not account for the warm/hot intergalactic medium (WHIM) frequently surrounding massive galaxies, as it was constructed before the first assessment of the WHIM by Cen & Ostriker (1999). The original G-KW model allows a prediction of the limiting (maximum) values for the source's age and linear size depending on the environment conditions, the jet power, and the cosmic epoch characterised by the source's redshift. However, our recent detections of very large-sized radio sources with $z > 1$ and exceeding the limits predicted by their model suggests that some of its free parameters should be modified.

In this paper an observational constraint for the G-KW model is analysed. For

this purpose, an effort in determining the largest sizes and dynamical ages of FRII-type radio sources at redshifts $1 < z < 2$ is undertaken. In Section 2, the original G-KW model is briefly described and modified adopting modern (contemporary) values for thermodynamic temperature and gas density of the two media. Then, the predicted relations between the sources' linear size and the age, as well as the expansion speed of the radio lobes' heads and the age are calculated. The observational data used to constrain the two-medium model are presented in Section 3. The small sample of the most distant giant-sized radio sources (Table 1 in Paper I) is revised and supplemented with two other limited samples of FRII-type sources comprising: (i) sources larger than 400 kpc within the redshift range $1 < z < 2$, most of them found in this paper, and (ii) selected 3CRR sources in majority smaller than 400 kpc at $z > 0.5$ forming a comparison sample of "normal"-sized radio sources. Physical parameters of the sample sources: the dynamical age, the jet power, the central radio-core density and the IGM density, and others, are derived using the DYNAGE algorithm (Machalski et al. 2007a). The application of this algorithm to the sample sources and the resulting values of the sources' parameters are described in Section 4. A comparison of the model predictions with the observational data is presented and discussed in Section 5.

For the purpose of calculating the linear size, volume and luminosity of the sample sources we use a Λ CDM model with cosmological parameters $\Omega_m=0.27$, $\Omega_\Lambda=0.73$ and $H_0=71 \text{ km s}^{-1} \text{ Mpc}^{-1}$.

2. The revised G-KW model

2.1. Base of the model

The jet's dynamics is governed by a balance between its thrust, $\Pi_{\text{jet}} \approx Q_{\text{jet}}/v_{\text{jet}}$ and the ram pressure force of the IGM, $\rho_a v_{\text{hs}}^2 A_{\text{hs}}$, where Q_{jet} is the jet power, v_{jet} is its velocity, ρ_a is the ambient medium gas density, v_{hs} is the speed of the jet's head (hot spot) with which it advances into the ambient medium, and A_{hs} is the cross-sectional area of the bow shock at the end of the jet. In the G-KW model, the jet propagates into a two-component medium comprised of:

– the gaseous halo with a power-law density profile $\rho_h(d) = \rho_0 [1 + (d/a_0)^2]^{-\delta}$ bound to the parent optical galaxy, where ρ_0 and a_0 are the density and the radius of the central radio core, respectively, and $\delta=5/6$. This distribution is assumed to be invariant with redshift. It is also assumed that this halo has nearly uniform electron temperature $(kT)_h$ [keV] (medium 1), and

– the surrounding hotter IGM of uniform density, ρ_{IGM} , with the temperature $(kT)_{\text{IGM}}(1+z)^2$ [keV] (medium 2).

Similarly to Gopal-Krishna & Wiita (1987) we have to assume characteristic values for the density and temperature of the considered media. The values adopted hereafter for the two components are based on the following data:

- (1) The radio core radius, $a_0=3$ kpc is based on the fitted X-ray surface-brightness

profile of nine nearby, low-luminosity radio galaxies recently observed by Croston et al. (2008). This value of the radius is derived from the observed angular radius of about 10 arcsec.

(2) The halos' gas temperature have been determined in a number of papers. A uniform temperature $(kT)_h=0.7$ keV was measured for a few nearby, X-ray luminous elliptical galaxies with the *Chandra Observatory* by Allen et al. (2006). Using *XMM-Newton* and *Chandra* observations, the values from 1 to 5 keV with a median of about 2.1 keV was found by Belsole et al. (2007) for the X-ray clusters surrounding 20 luminous 3CRR radio sources. For the low-luminosity radio galaxies analysed by Croston et al. (2008), a median of the fitted temperatures is about 1.4 keV.

(3) The halos' gas (proton) density of $(1-2) \times 10^4 \text{ m}^{-3}$ is fitted to X-ray counts by Belsole et al. (2007).

The interface between the X-ray halo and IGM is determined balancing the IGM pressure against the pressure distribution in the halo. A non-relativistic gas in thermal equilibrium that has an electron density $n_e [\text{m}^{-3}]$ and temperature $(kT)_e [\text{keV}]$ will have an electron pressure $p_e = n_e (kT)_e [\text{Pa}]$. Expressing electron density by the mass density, $\rho = n \mu m_H$, this balance will have place at the halo's radius R_h calculated from

$$\frac{\rho_0}{\mu_h m_H} [1 + (R_h/a_0)^2]^{-\delta} (kT)_h = \frac{\rho_{\text{IGM}}}{\mu_{\text{IGM}} m_H} (kT)_{\text{IGM}}, \quad (1)$$

where μ and m_H are the mean molecular weight and the mass of hydrogen atom, respectively. In this paper we assume $\mu_h=0.5$ and $\mu_{\text{IGM}}=1.4$. Besides, for the halo (medium 1) we adopt $n_p=1.5 \times 10^4 \text{ m}^{-3}$, i.e. a mean proton density of the values given by Belsole et al. (2007), which corresponds to $\rho_0=10^{-22.6} \text{ kg m}^{-3}$, and the temperature $(kT)_h=1.4$ keV. For the IGM density we take 50% of the cosmic matter density, i.e. $\rho_{\text{IGM}}=0.5\Omega_m h^2 \rho_{\text{clos}} = 0.5 \times 0.27 \times 0.71^2 \times (3H_0^2)/(4\pi G)$, which gives $\rho_{\text{IGM}}=10^{-26.9} \text{ kg m}^{-3}$. For the IGM temperature we adopt $(kT)_{\text{IGM}}=25$ keV. Substituting the above values into Eq. (1) we find $R_h=642$ kpc. This radius of X-ray halo is compatible with the radii determined by Cassano et al. (2007) for 15 Abell cluster radio halos with the mean of $\sim 560 \pm 170$ kpc. This is worth to notice that our radius of 642 kpc is much larger than 171 kpc used by Gopal-Krishna & Wiita. In an expanding and uniform IGM this radius should evolve as $R_h(z) = 642(1+z)^{-5/(2\delta)}$ kpc, i.e. $642(1+z)^{-3}$ kpc for $\delta=5/6$.

Fig.1 (a), (b), (c) present the basic characteristics of the two-media model: the mass density $\rho(d)$, the electron temperature $kT(d)$, and the resulting electron gas pressure $p(d)$, as functions of the distance from the host galaxy (compact radio core), respectively. Note that the balance $p_h(R_h) = p_{\text{IGM}}$ at $d = R_h$ corresponds to a rapid transition between $\rho(R_h)$ and ρ_{IGM} , as well as between $kT(R_h)$ and kT_{IGM} , and causes an unphysical effect shown in Section 5.1. The dashed curves in Fig.1 (a) and (b) indicate desired smooth transitions between the relevant parameters

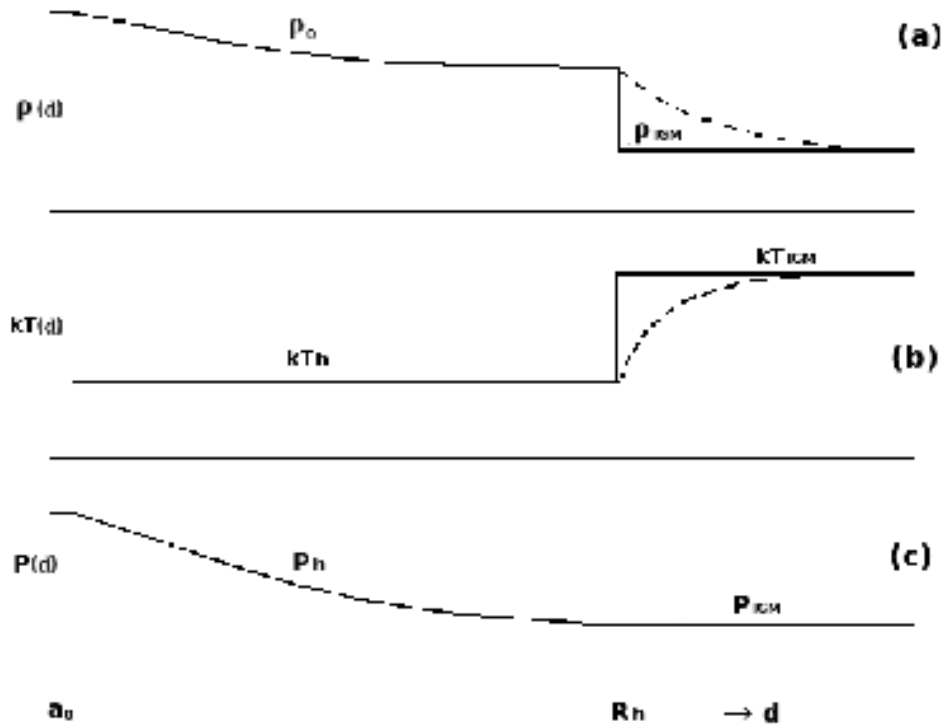


Fig. 1. Properties of the two-media environment surrounding the center of radio galaxy.

which would introduce a better physical scenario into the model.

2.2. Predictions of the model

For $d \leq R_h$ it is assumed that the jet propagate (through the medium 1) with a constant opening angle, θ . Under this condition, the ram pressure balance results in the following dependence for the jet length (the radio lobe size, D_ℓ) on time (the lobe's age, t) and the jet's head expansion velocity, v_h , on D_ℓ or t :

$$D_\ell(t) = [(2 - \delta)At]^{1/(2-\delta)}, \tag{2}$$

$$v_h(D_\ell) = AD_\ell^{(\delta-1)}, \tag{3}$$

$$v_h(t) = \left[(2 - \delta)A^{1/(\delta-1)}t \right]^{\frac{\delta-1}{2-\delta}}, \tag{4}$$

where

$$A \equiv \left(\frac{4c_1 Q_{\text{jet}}}{\pi \theta^2 c \rho_0 a_0^{2\delta}} \right)^{1/2}.$$

Here c_1 is a constant with a value between 1.5 and 3.8 depending on the source's (lobe's) geometry described by its axial ratio R_T (cf. Kaiser & Alexander 1997), while $c \approx v_{\text{jet}}$ is the speed of light. The jet's opening angle is also described by R_T , $\theta^2 = c_2/(4R_T)$, where c_2 is a constant with a value between 3.6 to 4.1 depending on specific heats for the material in the jet and the lobe (cocoon), (Eq. 17 in Kaiser & Alexander 1997).

At $d = R_h(z)$ the jet enters the hotter IGM (medium 2) at least an order of magnitude less dense but pressure-matched, as shown in Fig. 1. In order to analyse the jet's propagation over this regime, Gopal-Krishna & Wiita have considered two likely extreme scenarios for the lobe's expansion:

— *Scenario A* where the jet opening angle, θ , is conserved. Due to a rapid decrease of the ambient density at the interface, $\rho_{\text{IGM}} \ll \rho_h(R_h)$, a sufficient ram-pressure will be provided only if the jet's head velocity, v_{hs} , increases abruptly at $d=R_h$ and then gradually approaches the $v \propto d^{-1}$ law expected for a constant density medium. In this scenario:

$$D_\ell(t) = \left\{ 2 \left(K(z) + a_0^\delta A \left[\frac{\rho_0}{\rho_{\text{IGM}}(1+z)^3} \right]^{1/2} t \right) \right\}^{1/2} \quad \text{and} \quad (5)$$

$$v_h(t) = a_0^\delta A \left[\frac{\rho_0}{\rho_{\text{IGM}}(1+z)^3} \right]^{1/2} / D_\ell(t), \quad (6)$$

where

$$K(z) = \frac{1}{2} R_h^2(z) - R_h^{(2-\delta)}(z) \frac{a_0^\delta}{2-\delta} \left[\frac{\rho_0}{\rho_{\text{IGM}}(1+z)^3} \right]^{1/2}$$

is a redshift-dependent constant providing that the time corresponding to $D_\ell=R_h$ in Eqs. 2 and 5 is the same.

— *Scenario B* where the jet's head velocity across the interface remains continuous and therefore matched to the value given by Eq. (3) for $D_\ell=R_h$. This can be achieved only with an abrupt flaring of the jet's opening angle. Under this condition the model predicts:

$$D_\ell(t) = \left\{ 2 \left(A R_h^\delta(z) t - R_h^2(z) \frac{\delta}{2(2-\delta)} \right) \right\}^{1/2} \quad \text{and}, \quad (7)$$

$$v_h(t) = A R_h^\delta(z) / D_\ell(t). \quad (8)$$

The sound speed in the IGM is given by

$$s_{\text{IGM}}(z) = \left[\frac{\Gamma(kT)_{\text{IGM}}}{\mu m_{\text{H}}} \right]^{1/2} (1+z). \quad (9)$$

Given the values $\Gamma=5/3$, $\mu=1.4$ and $(kT)_{\text{IGM}}=25$ keV, the sound speed limiting the source (lobe) axial expansion velocity is $s_{\text{IGM}} \approx 0.0056c$ at $z \approx 0$, and $s_{\text{IGM}} \approx 0.0169c$ at $z \approx 2$.

The time dependence of the source size $D_\ell(t)$ calculated from Eqs. 2, 5 and 7, as well as of the axial expansion velocity $v(t)$ calculated from Eqs. 4, 6 and 8 for the three cases: $Q_{\text{jet}}=10^{37.5}$ W and $z=0.5$, $Q_{\text{jet}}=10^{38.5}$ W and $z=1.0$, and $Q_{\text{jet}}=10^{39.5}$ W and $z=2.0$, are shown in Fig. 5 and Fig. 6, respectively.

To compare these predictions with the observations, we select three different samples of FR II-type radio sources.

3. Selection of the samples

3.1. Sample 1 (GRS sample)

The revised sample of FR II-type radio sources with $0.5 < z < 1$ and the projected linear size larger than 1 Mpc, compiled from the literature, is presented in Table 1. Columns (1)–(5) are self explanatory. Entries in columns (6)–(10) are the data used to determine the age and other physical parameters of the sample sources in Section 4. These are: R_{T} – axial ratio of the source, ϕ – assumed orientation angle of the jet axis, and P_{v} – monochromatic luminosity of the source at the given low, medium, and high frequency, respectively (cf. Section 4.1). Some necessary references are given in the Notes.

3.2. Sample 2 (Distant-source sample)

The second sample of FR II-type sources larger than 400 kpc and having $z > 1$ consists of a few sources known from the literature and the sources found in this paper. The latter part of this sample results from the dedicated research project attempting to determine how large linear size FR II-type radio sources can achieve at redshifts $1 < z < 2$. This part was preselected using the modern Sloan Digital Sky Survey (hereafter referred to as SDSS: Adelman-McCarthy et al. 2007) as the finding survey. The optical objects extracted from the SDSS, fulfilling the above redshift criterion and classified either as a galaxy (G) or a QSO (Q), were then cross-correlated with the radio 1400-MHz sky survey FIRST (Becker, White & Helfand 1995). In the second step, all optical objects strictly coinciding (within an angular separation less than 0.5 arcsec) with a compact radio source, i.e. with a potential radio core, were subject to the further selection. In the third step, we have checked whether the (core) component is surrounded by a pair of nearly symmetric, possibly extended radio structures (lobes) with an angular separation providing a projected linear size $D \gtrsim 400$ kpc. All candidates were verified by an inspection of their images (if exist) in other available radio surveys, namely the 1400-MHz NVSS

Table 1

The sample of FR II-type sources with $0.5 < z < 1$ and $D > 1$ Mpc. The radio luminosities are given in units of $W/(\text{Hz} \cdot \text{sr})$. The low-frequency luminosity, P_{lf} , is determined either at 74 MHz (marked a) or 151 MHz (b) or 325 MHz (c).

IAU name	Survey	z	Id.	D [kpc]	R_T	ϕ [$^\circ$]	$\log P_{lf}$	$\log P_{1400}$	$\log P_{4850}$	Notes
(1)	(2)	(3)	(4)	(5)	(6)	(7)	(8)	(9)	(10)	(11)
J0037+0027		0.5908	G	1976	5.0	90	26.103 ^a	25.149	24.606	(4, 5)
B0654+482	7C	0.776	G	1002	4.0	90	26.120 ^b	25.262	24.733	(1)
J0750+656		0.747	Q	1606	4.0	90	26.189 ^a	25.255	24.715	(3)
B0821+695	8C	0.538	G	2580	3.0	90	26.142 ^b	25.106	24.525	(2)
B0854+399	B2	0.528	G	1014	2.7	70	26.385 ^b	25.627	25.098	
B1058+368	7C	0.750	G	1100	4.2	90	26.192 ^b	25.412	24.809	(1)
J1130–1320	PKS	0.6337	Q	2033	3.8	90	27.275 ^a	26.198	25.613	(4, 5)
B1602+376	7C	0.814	G	1376	2.6	90	26.292 ^b	25.486	24.936	(1)
B1636+418	7C	0.867	G	1004	3.9	90	26.006 ^b	25.273	24.701	(1)
B1834+620	WNB	0.5194	G	1384	4.1	90	26.361 ^b	25.555	25.067	(6)
J1951+706		0.550	G	1300	4.5	90	25.974 ^a	24.894	24.448	(3)
J2234–0224		0.55	Q	1266	4.5	90	—	24.840	—	(4, 5)

Notes: (1)–Cotter et al. (1996); (2)–Lara et al. (2000); (3)–Lara et al. (2001); (4)–Koziel-Wierzbowska (2008); (5)–Machalski et al. (2007b); (6)–Schoenmakers et al. (2000)

(Condon et al. 1998), 325-MHz WENSS (Rengelink et al. 1997), and 74-MHz VLSS (Cohen et al. 2007). The assumed cosmology (cf. Introduction) predicts that a maximum of the linear size/angular size quotient at $z > 1$ is ~ 8.55 kpc/arcsec which, in turn, implies that a source larger than 400 kpc should have an angular size $LAS \gtrsim 47$ arcsec. All radio sources selected this way from the SDSS are classified as QSO. The final sample is presented in Table 2. All columns give the similar data as those in Table 1. The radio images of exemplary sample sources, made using combined data from the NVSS and FIRST surveys, are shown in Figs. 2–4. The precise coordinates, angular sizes and 1400 MHz total flux densities, taken from NVSS catalogue, are given in the Appendix (Table 8).

However, in order to use this sample to constrain the analytical G-KW model, besides the redshift and linear size of the member sources, we have to determine their age and other physical parameters which is not attainable without an information about the radio spectrum within wide-enough spectral range and providing the radio luminosity of a given source at least three or more different observing frequencies. For the large part of the Sample 2 we were able to use flux densities from the radio catalogues: VLSS (74 MHz), 6C and 7C (151 MHz; Hales et al. 1988 and Riley et al. 1999, respectively), WENSS (325 MHz), B3 (408 MHz; Ficarra et al. 1985, NVSS (1400 MHz) and GB6 (4850 MHz; Gregory et al. 1996). It is worth to notice that three QSOs in Sample 2 have (projected) linear size larger than 1 Mpc!

Table 2

The sample of FR II-type sources with $1 < z < 2$ and $D > 400$ kpc. The low-frequency luminosity marked *a*, *b*, *c* – as in Table 1. The values in parenthesis are approximated because of less certain subtraction of the core contribution

IAU name	Survey	<i>z</i>	Id.	<i>D</i> [kpc]	<i>R</i> _T	ϕ [$^\circ$]	log <i>P</i> _{lf}	log <i>P</i> ₁₄₀₀	log <i>P</i> ₄₈₅₀	Notes
(1)	(2)	(3)	(4)	(5)	(6)	(7)	(8)	(9)	(10)	(11)
J0245+0108		1.537	Q	456	3.6	70	27.822 ^a	26.658	26.087	
J0809+2015		1.129	Q	465	3.1	70	—	(25.61)	(25.02)	(1)
J0809+2912		1.481	Q	1120	3.0	70	27.234 ^a	26.476	26.015	
J0812+3031		1.312	Q	1240	3.0	70	25.504 ^c	25.032	—	(2)
J0819+0549		1.701	Q	985	3.0	70	—	25.578	—	(1, 2)
J0839+2928		1.136	Q	417	2.3	45	26.813 ^a	25.882	25.364	
J0842+2147		1.182	Q	1080	3.0	70	—	25.425	—	(1, 2)
J0857+0906		1.688	Q	506	4.5	70	27.357 ^a	26.276	25.763	
J0902+5707		1.595	Q	862	4.0	70	25.905 ^c	25.325	—	(2)
J0906+0832		1.617	Q	682	3.6	70	—	25.750	—	(1, 2)
J0947+5154		1.063	Q	478	3.9	70	27.002 ^a	25.767	25.157	
J0952+0628		1.362	Q	551	4.3	70	27.081 ^a	25.988	25.508	
B1011+365	6C	1.042	G	416	3.5	70	26.902 ^b	26.204	25.680	
J1030+5310		1.197	Q	835	3.0	90	26.336 ^b	25.481	24.945	
J1039+0714		1.536	Q	501	3.0	70	—	25.450	—	(1, 2)
B1108+359	3C252	1.105	G	493	3.0	70	28.164 ^a	26.921	26.282	
B1109+437	B3	1.664	Q	488	4.5	70	28.092 ^a	27.357	26.812	
J1130+3628		1.072	Q	422	3.0	50	25.992 ^b	25.277	(24.67)	
J1207–0244		1.100	Q	444	3.0	50	26.590 ^a	25.407	—	(2)
J1434–0123		1.020	Q	490	3.0	50	26.894 ^a	25.763	—	(2)
J1550+3652		2.061	Q	675	3.0	70	26.771 ^b	26.041	25.527	
J1706+3214		1.070	Q	438	3.0	50	26.757 ^a	25.682	25.150	
B1723+510	3C356	1.079	G	614	4.0	70	27.875 ^b	26.916	26.304	
J2345–0936		1.275	Q	513	3.2	90	27.318 ^a	26.266	(25.62)	
B2352+796	3C469.1	1.336	G	626	4.4	70	28.269 ^a	27.167	26.628	

Notes: (1)–off the 7C and WENSS surveys; (2)–off the 4850-MHz GB6 or PMN6 (Griffith et al. 1995) surveys or below their flux density limit

3.3. Sample 3 (3CRR sample)

The third observational sample comprises 3CRR FR II-type sources with $z > 0.5$ but size smaller than 400 kpc (except of 3C265 and 3C292 which are larger). For the reason to have homogeneous and complete data for radio spectra of the sample sources necessary for estimation of their dynamical age and corresponding physical parameters (jet power, mean expansion velocity, etc.), this sample is limited to sources with the Galactic latitude of $\delta_{\text{II}} > 30^\circ$ where good spectral data are available from the low-frequency radio surveys: VLSS, 6C, 7C and WENSS. The sample sources are presented in Table 3.

4. Ageing analysis of the samples' sources

4.1. Application of the DYNAGE algorithm

The dynamical age analysis is performed using the DYNAGE algorithm of Machalski et al. (2007a). It is based on the analytical KDA model (cf. Introduction). The original KDA model, assuming values for a number of free parameters of the model (e.g. the jet power Q_{jet} , radius a_0 and density ρ_0 of the radio core, exponent β in the power-law density distribution in the external medium $\rho(d/a_0)^{-\beta}$, and the effective injection spectral index α_{inj} , which approximates the initial relativistic particle continuum at a head of the jet $n(\gamma_i) = n_0(\gamma_i^{-p})$, where γ_i is the Lorentz factor of these particles and $p = (\alpha_{\text{inj}} + 1)/2$), allows prediction of a time evolution of the source's parameters, e.g. its length, $D(t)$, and radio luminosity, $P_V(t)$, at a given observing frequency – as a function of its assumed age t .

Oppositely, the DYNAGE algorithm enables solving a reverse problem, i.e. finding the values of t , α_{inj} , Q_{jet} , and ρ_0 for a real source. Determining the values of these four free parameters of the model is possible by a fit to the observational parameters of a source: its projected linear size D , the volume V , the radio monochromatic luminosity P_V , and the radio spectrum α_ν that provides $P_{V,i}$ at a number of observing frequencies $i = 1, 2, 3, \dots$. To determine these luminosities for the sample sources, we have had to fix the flux density in their lobes at a number of frequencies, i.e. to subtract a flux contribution from the compact components such as the radio core and hot spots in these lobes. This was especially important for the sample sources identified with quasars. The resulting luminosities at three observing frequencies: the lowest frequency used (74, 151, or 325 MHz), the medium one of 1400 MHz, and the highest one of 4850 MHz, are given in columns (8)–(10) in Tables 1 and 2, as well as in columns (7)–(9) in Table 3.

As in KDA, we adopted a cylindrical geometry of the source's cocoon (radio lobes) where its volume is determined by the deprojected length $D/\sin\phi$ and the axial ratio R_T . The values of R_T are estimated from the low-frequency radio images, and an angle of orientation of the jet axis to the observer's line of sight, ϕ , is subjectively estimated from the observed asymmetry in the lobes' arms and brightness. The values of these two parameters are given in columns (6) and (7) of Tables 1 and 2, and in columns (5) and (6) in Table 3.

Unfortunately, the values of other free parameters of the model have to be assumed. These are: $\gamma_{i,\text{min}} = 1$ and $\gamma_{i,\text{max}} = 10^7$ that are the Lorentz factors determining the energy range of the relativistic particles used in integration of their initial power-law distribution; Γ_j , Γ_x , Γ_B , and Γ_c , are all equal to 5/3, are the adiabatic indices in the equation of state for the jet material, the unshocked medium surrounding the lobes, a "magnetic" fluid, and the source (cocoon) as a whole, respectively; and $k' = 0$ is the ratio of the energy density of thermal particles to that of the relativistic particles. The more detailed description of application of the above algorithm to observed radio structures is published in Machalski et al. (2009).

4.2. Results of the modelling

The resulting values of the age and other physical parameters of the sample sources are given in Tables 4, 5 and 6 (for the Sample 1, 2 and 3, respectively). Columns (2) and (3) give the dynamical age, t , and the effective, initial slope of the radio spectrum α_{inj} . Columns (4) – (7): (in the logarithmic scale) the jet power, Q_{jet} , the central core density, ρ_0 , the pressure along the jet axis, p_h , and the total energy radiated out during the age of source, U_c . The age t and the fitted values of Q_{jet} and ρ_0 fulfil the dynamical equation

$$t = \left(\frac{D}{2c_1 \sin \phi} \right)^{\frac{5-\beta}{3}} \left(\frac{\rho_0 a_0^\beta}{Q_{\text{jet}}} \right)^{1/3}, \quad (10)$$

Where $D/(2 \sin \phi) \equiv D_\ell$ is the deprojected length of a given lobe treated here as one half of the total, observed size of the source, D . The energy density fulfilling the energy equipartition condition is calculated from

$$u_{\text{eq}}(t) = \frac{18c_1^{(2-\beta)}}{(\Gamma_x + 1)(\Gamma_c - 1)(5 - \beta)^2 \mathcal{P}_{\text{hc}}} \left(\rho_0 a_0^\beta \right)^{\frac{3}{5-\beta}} Q_{\text{jet}}^{\frac{2-\beta}{5-\beta}} t^{-\frac{4+\beta}{5-\beta}}, \quad (11)$$

where $\mathcal{P}_{\text{hc}} = (2.14 - 0.52\beta)R_T^{2.04-0.25\beta}$ is the empirical formula for the pressure ratio along the jet axis and the transverse direction taken from Kaiser (2000). The total radiated energy is simply $U_c = u_{\text{eq}} \times V_c$, where the source (cocoon) volume attained at the age t is $V_c = (\pi/4)D^3/(2R_T)^2$. Column (8) gives the magnetic field strength estimate derived from

$$B = \left(\frac{24}{7} 10^{11} \pi u_B \right)^{1/2} [\text{nT}], \quad (12)$$

where the magnetic field energy density is $u_B = u_{\text{eq}}(1+p)/(5+p)$. The last column (9) gives the actual expansion velocity of the lobe's head along the jet axis which is the derivative of the D_ℓ function

$$v_h(t) = \frac{dD_\ell}{dt} = \frac{3c_1}{5-\beta} \left(\frac{Q_{\text{jet}}}{\rho_0 a_0^\beta} \right)^{\frac{1}{5-\beta}} t^{\frac{\beta-2}{5-\beta}}. \quad (13)$$

5. Observational constrain for the model

5.1. Comparison of the model's prediction with the observational data

The model's predictions, i.e. the dependence of the deprojected linear size and the jet's head velocity on the source's age ($D/\sin\phi$ vs t and v_h/c vs t , respectively), are compared with the data determined for the sampled sources and given in Tables 4, 5 and 6. Fig. 5 shows the dependence of $D/\sin\phi$ on t . The model's predictions

are presented for three different sets of values of the jet power and redshift: $z = 0.5$ and $Q_{\text{jet}} = 10^{37.5}$ W, $z = 1$ and $Q_{\text{jet}} = 10^{38.5}$ W, $z = 2$ and $Q_{\text{jet}} = 10^{39.5}$ W, marked "1", "2", and "3", respectively. The above dependence predicted in the frame of scenario A are drawn with the solid lines, while these for scenario B – with the dashed lines. The points of bifurcation of the model's predictions into scenario A and scenario B correspond to the halo diameter dependent on redshift, $2R_h(z)$ (on the ordinate axis) and to the related age (on the abscissa axis). The ends of both solid and dashed lines indicate a maximum size and age at which the predicted expansion velocity reaches the speed of sound. The crosses show the distribution of the GRSs from Sample 1, the full circles – the distant sources (mostly QSOs) from Sample 2, and the open circles – the 3CRR sources from Sample 3.

The dependence of v_h/c on t is shown in Fig. 6. The model's predictions and the sample sources are indicated with the lines and symbols as in Fig. 5. The rapid increase of v_h/c in the frame of scenario A results from the discontinuities of $\rho(d)$ and $kT(d)$ at the halo-IGM interface (cf. Fig. 1). The three horizontal dotted lines indicate the predicted lower values of the axial expansion velocity, $v_{h,\text{min}}/c$, limited by the sound speed at the given values of redshift.

The maximum size which any FR II-type radio source can reach with a given value of $v_{h,\text{min}}/c$, (i.e. at the corresponding redshift) depends on the jet power. The size D_{max} in the frame of scenario A, as a function of $v_{h,\text{min}}/c$ (or z), is plotted on Fig. 7 for three values of Q_{jet} considered above.

5.2. Age and physical parameters of the sample sources

The three samples used differ significantly in the distribution of fitted age of their members. A median of age in the Sample 1, 2 and 3 is 65 ± 8 Myr, 22 ± 2.5 Myr, and 4 ± 1 Myr, respectively. A median linear size in these samples is ~ 1330 kpc, ~ 510 kpc, and ~ 145 kpc, respectively. As the Samples 1 and 2 comprise the largest sources (of FR II type only) each of them in different redshift range, and this range in the Sample 2 is twice the range of the Sample 1 – we compare the $D - z$ dependence for these sources with that found in other samples unlimited in linear size of their members (e.g. Eales 1985; Barthel & Miley 1988). Since the Sample 1, i.e. the sample of known high-redshift GRSs, is very small and consists of 12 sources only, below we also consider 12 of the largest ones from the Sample 2. The relevant medians are: $D_{\text{med}} = 1330 \pm 120$ kpc at $z_{\text{med}} = 0.60 \pm 0.10$, and $D_{\text{med}} = 760 \pm 80$ kpc at $z_{\text{med}} = 1.35 \pm 0.20$, respectively. Assuming that $D_{\text{med}} \propto (1+z)_{\text{med}}^{-n}$, we find $n \approx 1.5$ which is compatible with a value of this power $\sim (1-2)$ determined in several samples of radio galaxies and quasars (e.g. Kapahi 1989). Therefore the above result agree with the trend observed in much more abundant samples of sources and confirms that the largest linear size, which a source can achieve before dimming below the detection limit, inevitably decreases with redshift irrespective of a cosmological evolution of the IGM (cf. Nilsson et al. 1993).

In order to enlighten the latter problem, we pay an attention to the pressure at

the head of lobes (along the jet's axis), p_h , given in column 6 of Tables 4, 5 and 6. This pressure is determined in the DYNAGE as

$$p_h = \mathcal{P}_{hc}(R_T)p_c(R_T, t),$$

where \mathcal{P}_{hc} is the pressure ratio (cf. Section 4.2), and $p_c = (\Gamma_c - 1)u_{eq}$, where u_{eq} is given by Eq. 11. The median of this pressure, $p_{h,med}$, for sources in the Sample 1 and Sample 2 is $\sim 10^{-12.0}$ N/m² and $\sim 10^{-10.8}$ N/m², respectively, thus a (mean) pressure at the head of lobes of the sources within the redshift range $z[1, 2]$ is about 16 times higher than that for the sources within $z[0.5, 1]$. If so, it is more than twice higher than a ratio implied from the formula giving pressure of a non-relativistic, homogeneous IGM in thermal equilibrium, $p(z) = p_0(1+z)^5$, where p_0 is the present-day pressure (Subrahmanyan & Saripalli 1993). We return to this point in the next section.

6. Discussion of the results and conclusions

The distribution of sources on the planes $D/\sin\phi - t$ and $V_h/c - t$ (in Fig. 5 and 6, respectively) is more or less compatible with model's prediction, however the samples used to constrain the model may be too small to be decisive. So, much larger samples of sources with reliably determined ages would support or impair the inferences drawn as follows:

(i) Scenario B is rather excluded because both the maximum size, $D_{max} \sim 600$ kpc, and the corresponding age, $t_{max} \sim 70$ Myr allowed by the model are evidently smaller and younger than the observed values of those parameters for the sample sources. Also high-dynamics radio observations show no evidence for a flaring of the jets in FR II-type sources; oppositely the jets in these sources are rather recollimated in vicinity of the radio core.

(ii) As expected, the inferred expansion velocity, v_h/c , of all the sources used to constrain the G-KW model are higher than the limiting sound speed marked in Fig. 6. This result confirms a common belief that the heads of lobes of FR II type sources are overpressured with respect to the external gaseous medium. We note that the lowest expansion velocities of the largest sources, i.e. these in the Samples 1 and 2, are comparable to those of much smaller sources in the Sample 3.

(iii) The age of the three sources in Sample 2 is probably underestimated and the corresponding expansion velocity – overestimated (the three full dots with $t < 10$ Myr and $v_h > 0.1c$ in Figs. 5 and 6) due to possible relativistic effects (cf. Arshakian & Longair 2000). All are classified as quasars, and the two of them (J0809+2912 and J1550+3652) are highly asymmetric in their lobes' brightness. If a probable anisotropic radiation is discerned and the proper luminosity of the cocoon is taken into calculations, the age of these sources would be older and the expansion velocity – lower than the values in Table 6.

(iv) The pressure in the diffuse lobes of the largest radio sources seems to offer a tool useful for an estimation of the IGM pressure. If the axial pressure in lobes of the largest observed sources, especially these in the Sample 2, is close to equilibrium with the IGM pressure, the inferred values of p_h would suggest even stronger density evolution of the IGM than $\rho_{\text{IGM}} \propto (1+z)^3$ (cf. Eqs. 5 and 6). However, radio images of the sources in the Sample 2 evidently indicate a presence of hot spots which, in turn, may confirm that the hot spot regions are highly overpressured with respect to the IGM, and the actual age of sources cannot be considered as a lifetime. Moreover, the DYNAGE fits show that the jet powers of the most distant sources are significantly higher than that for sources of a similar age but at low redshifts $z < 0.2$. As it was shown in Section 5.2, the median age in the Sample 2 is ~ 22 Myr. An inspection of the compilation of over 200 radio galaxies and quasars with the dynamical ages fitted using the DYNAGE method (the data unpublished yet) resulted in only 7 radio galaxies of age of about 25 Myr and lying within the redshift range $z[0.1, 0.2]$. These galaxies and their observational and dynamical parameters are listed in Table 7.

The median jet power, $Q_{\text{jet,med}}$, in the Sample 2 (cf. Table 5) is $\sim 1.8 \times 10^{39}$ W, while that for the galaxies in Table 8 is $\sim 2.8 \times 10^{37}$ W. We argue that this is very unlikely to find so young FR II type radio sources at redshift below 0.2 and driven by jets more powerful than 10^{38} W. Although this may be partly caused by the selection effect. In fact, searching for high-redshift sources we probe a much larger space volume than the volume corresponding to a low redshift. Probably therefore this is why the only low-redshift and very powerful radio galaxy known is Cygnus A with $t \approx 8$ Myr, $D = 135$ kpc, and $Q_{\text{jet}} \approx 1.4 \times 10^{39}$ W (cf. Machalski et al. (2007a), the above result strongly suggests that the dynamical evolution of FR II type radio sources at high redshifts (in earlier cosmological epochs) is different and faster than that of sources at low redshifts. The model constrained in this paper implies that giant-sized sources (with $D > 1$ Mpc) can exist at redshifts as high as ~ 2 , however only if their jets are powerful enough.

(v) A differentiation of the jet's (highest) power at high and low redshifts perhaps would be a strong argument for the theoretical speculations about its dependence on the properties of a black hole (BH) in AGN: the spin of the BH (Blandford & Znajek 1977) and/or the accretion process and its rate (Sikora, Stawarz & Lasota 2007; Sikora 2009). This is very likely that the accretion of matter onto the BH must play a dominant role in the jets' production. This led to a presumption that more powerful jets can be due to a larger amount of material available for the accretion processes inside AGN formed at earlier cosmological epochs.

Reasuming the above we can conclude as follows:

— An observational quest for the largest radio sources of FR II type at high redshifts $1 < z < 2$ resulted in the sample of 25 sources listed in Table 2, where 20 of 25 are found in this paper. Because the finding sky survey used was the optical SDSS survey, all the newly radio-identified optical objects appear to be

quasars with the (projected) linear size from ~ 400 kpc to ~ 1200 kpc. The above bias precluded a detection of large, most distant and low-luminosity radio galaxies whose parent optical counterpart will likely be of $\sim (22-24)$ R mag.

— Though the samples used to constrain the model are small, the observational data seem to be concordant with the predictions in the frame of Scenario A. However much larger samples of distant sources with reliably determined ages will be more decisive for the above aim.

— The derived lowest values of the lobes' head pressure, p_h , evidently higher than the limiting sound speed at different redshifts, strongly suggest that heads of even the largest sources at high redshifts are still overpressured with respect to the IGM.

— An existence of giant-sized radio sources at high redshifts is possible due to extremely high power of their jets up to $\sim 10^{40}$ W. Such the highest jet powers are likely related to the accretion processes onto massive black holes in the central AGN, which might be very efficient in the nuclei formed at earlier cosmological epochs.

7. Appendix

Table 8 gives precise sky coordinates of the parent optical object selected from the SDSS survey and identified with the given radio source, its (largest) angular size measured in the FIRST images, and the 1400-MHz total flux density taken from the NVSS catalogue.

Acknowledgements. This project was supported by the MNiSW with funding for scientific research in years 2009–2012 under contract No. 3812/B/H03/2009/36. Funding for the SDSS and SDSS-II has been provided by the Alfred P. Sloan Foundation, the Participating Institutions, the National Science Foundation, the U.S. Department of Energy, the National Aeronautics and Space Administration, the Japanese Monbukagakusho, the Max Planck Society, and the Higher Education Funding Council for England. The SDSS Web Site is <http://www.sdss.org/>.

The authors are grateful to the anonymous referee for valuable remarks and suggestions that helped to improve the paper.

REFERENCES

- Allen, S.W., Dunn, R.J.H., Fabian, A.C., Taylor, G.B., and Reynolds, C.S. 2006, *MNRAS*, **372**, 21.
 Adelman-McCarthy, J.K., Agüeros, M.A., Allam, S.S., Anderson, K.S.J., et al. 2007, *Astrophys. J. Suppl. Ser.*, **172**, 634.
 Arnaud, K.A., Fabian, A.C., Eales, S.A., Jones, C., and Forman, W. 1984, *MNRAS*, **211**, 981.
 Arshakian, T.G., and Longair, M.S. 2000, *MNRAS*, **311**, 846.
 Barthel, P.D., and Miley, G.K. 1988, *Nature*, **333**, 319.
 Becker, R.H., White, R.L., and Helfand, D.J. 1995, *Astrophys. J.*, **450**, 559.
 Begelman, M.C., and Cioffi, D.F. 1989, *Astrophys. J.*, **345**, L21.

- Belsole, E., Worrall, D.M., Hardcastle, M.J., and Croston, J.H. 2007, *MNRAS*, **381**, 1109.
- Blandford, R.D., Znajek, R. 1977, *MNRAS*, **179**, 433.
- Cassano, R., Brunetti, G., Setti, G., Govoni, F., and Dolag, K. 2007, *MNRAS*, **378**, 1565.
- Cen, R., Ostriker, J.P. 1999, *ApJ*, **514**, 1.
- Cohen, A.S., Lane, W.M., Cotton, W.D., Kassim, N.E., et al. 2007, *Astron.J.*, **134**, 1245.
- Condon, J.J., Cotton, W.D., Greiser, E.W., Yin, Q.F., et al. 1998, *Astron.J.*, **115**, 1693.
- Cotter, G. 1998, *Astrophysics and space science library (ASSL)*, Eds. M.N. Bremer et al. (Dordrecht: Kluwer Academic Publishers), p. 233.
- Cotter, G., Rawlings, S., and Saunders, R. 1996, *MNRAS*, **281**, 1081.
- Croston, J.H., Hardcastle, M.J., Birkinshaw, M., Worrall, D.M., and Laing, R.A. 2008, *MNRAS*, **386**, 1709.
- Eales, S.A. 1985, *MNRAS*, **217**, 149.
- Falle, S.A.E.G. 1991, *MNRAS*, **250**, 581.
- Ficarra, A., Grueff, G., and Tomassetti, G. 1985, *Astron. Astrophys. Suppl. Ser.*, **59**, 255.
- Gopal-Krishna, and Wiita, P.J. 1987, *MNRAS*, **226**, 531.
- Gregory, P.C., Scott, W.K., Douglas, K., and Condon, J.J. 1996, *Astrophys.J. Suppl. Ser.*, **103**, 427.
- Griffith, M.R., Wright, A.E., Burke, B.F., and Ekers, R.D. 1995, *Astrophys. J. Suppl. Ser.*, **97**, 347.
- Hales, S.E.G., Baldwin, J.E., and Warner, P.J. 1988, *MNRAS*, **234**, 919.
- Kaiser, C.R. 2000, *Astron. Astrophys.*, **362**, 447.
- Kaiser, C.R., and Alexander, P. 1997, *MNRAS*, **286**, 215.
- Kaiser, C.R., Dennett-Thorpe, J., and Alexander, P. 1997, *MNRAS*, **292**, 723.
- Koziel-Wierzbowska, D. 2008, *Ph D Thesis, Jagellonian Univ.*, Kraków.
- Kapahi, V.K. 1989, *Astron.J.*, **97**, 1.
- Lara, L., Mack, K.-H., Lacy, M., Klein, U., Cotton, W.D., et al. 2000, *Astron. Astrophys.*, **356**, 63.
- Lara, L., Cotton, W.D., Feretti, L., Giovannini, G., Marcaide, J.M., et al. 2001, *Astron. Astrophys.*, **370**, 409.
- Machalski, J., Chyży, K.T., Stawarz, L., and Koziel, D. 2007a, *Astron. Astrophys.*, **462**, 43.
- Machalski, J., Jamrozy, M., Saikia, D.J. 2009, *MNRAS*, **395**, 812.
- Machalski, J., Koziel-Wierzbowska, D., and Jamrozy, M. 2007b, *Acta Astron.*, **57**, 227. Paper I
- Machalski, J., Koziel-Wierzbowska, D., Jamrozy, M., and Saikia, D.J. 2008, *Astrophys. J.*, **679**, 149.
- McGilchrist, M.M., Baldwin, J.E., Riley, J.M., Titterton, D.J., et al. 1990, *MNRAS*, **246**, 110.
- Nilsson, K., Valtonen, M.J., Kotilainen, J., and Jaakkola, T. 1993, *ApJ*, **413**, 453.
- Rengelink, R.B., Tang, Y., de Bruyn, A.G., Miley, G.K., et al. 1997, *Astron. Astrophys. Suppl. Ser.*, **124**, 259.
- Riley, J.M.W., Waldram, E.M., and Riley, J.M. 1999, *MNRAS*, **306**, 31.
- Schoenmakers, A.P., de Bruyn, A.G., Röttgering, H.J.A., van der Laan, H. 2000, *MNRAS*, **315**, 395.
- Sikora, M. 2009, *Astron. Nachr.*, **330**, 291.
- Sikora, M., Stawarz, L., and Lasota, J.P. 2007, *ApJ*, **658**, 815.
- Subrahmanyam, R., and Saripalli, L. 1993, *MNRAS*, **260**, 908.

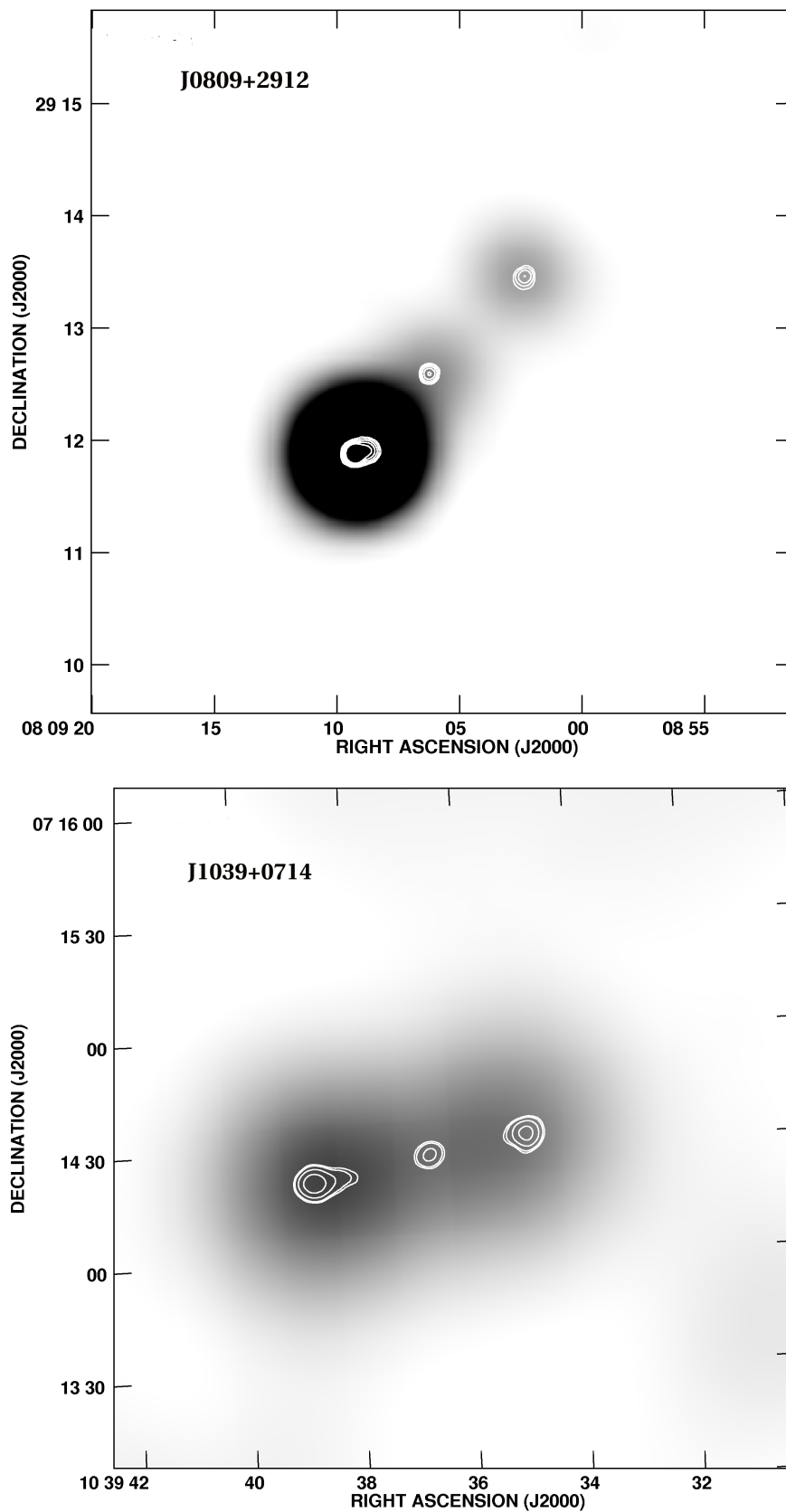


Fig. 2. 1400 MHz VLA maps of the sources J0809+2912 and J1039+0714. The NVSS images (gray scale) are combined with the FIRST contour maps. Total intensity, logarithmic contours are spaced by a factor of 2, starting with a value of 1.0 mJy/beam (except J1434-0123 starting with 0.2 mJy/beam).

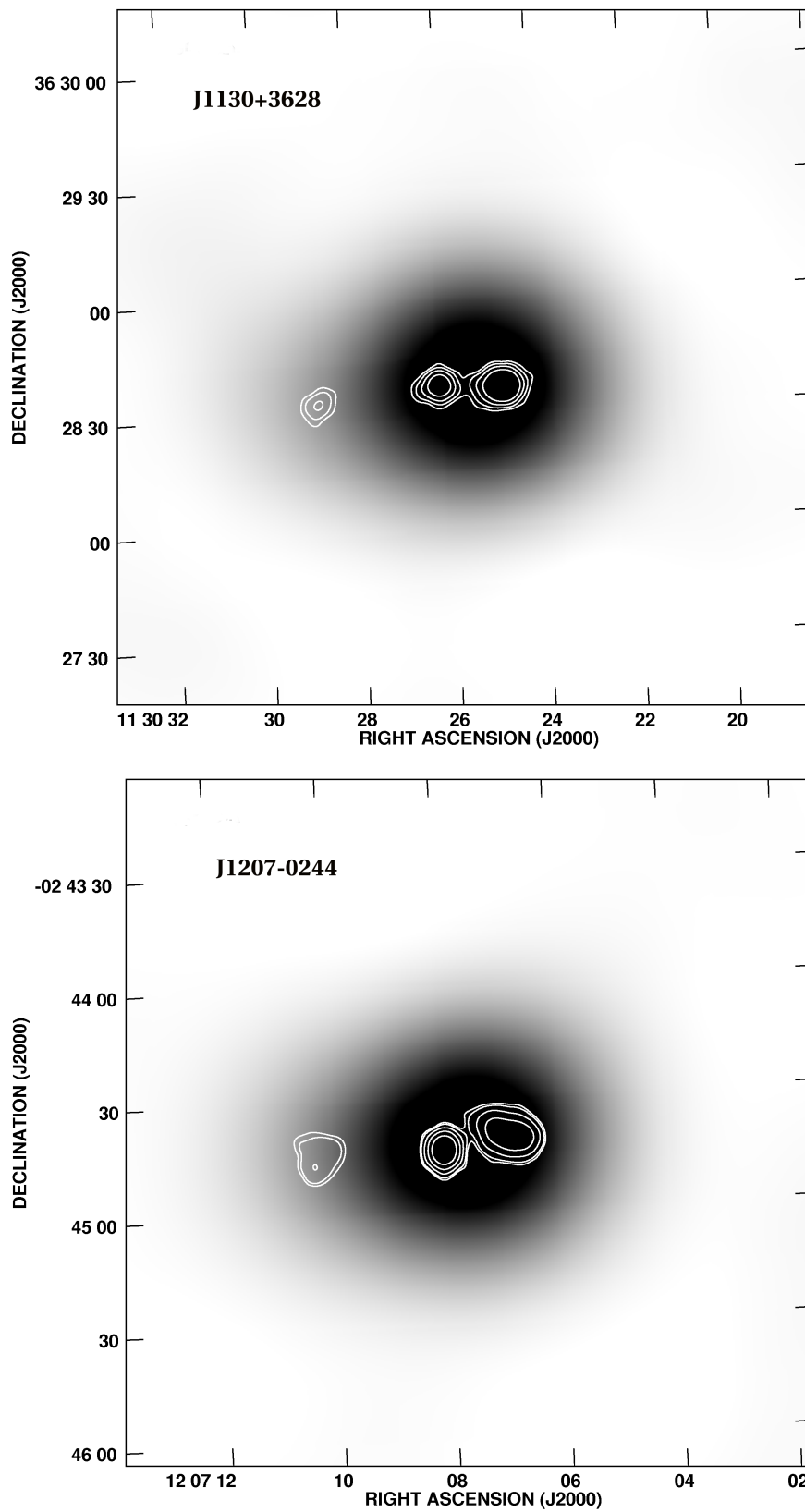


Fig. 3. The same as in Fig.2 but for J1130+3628 and J1207-0244

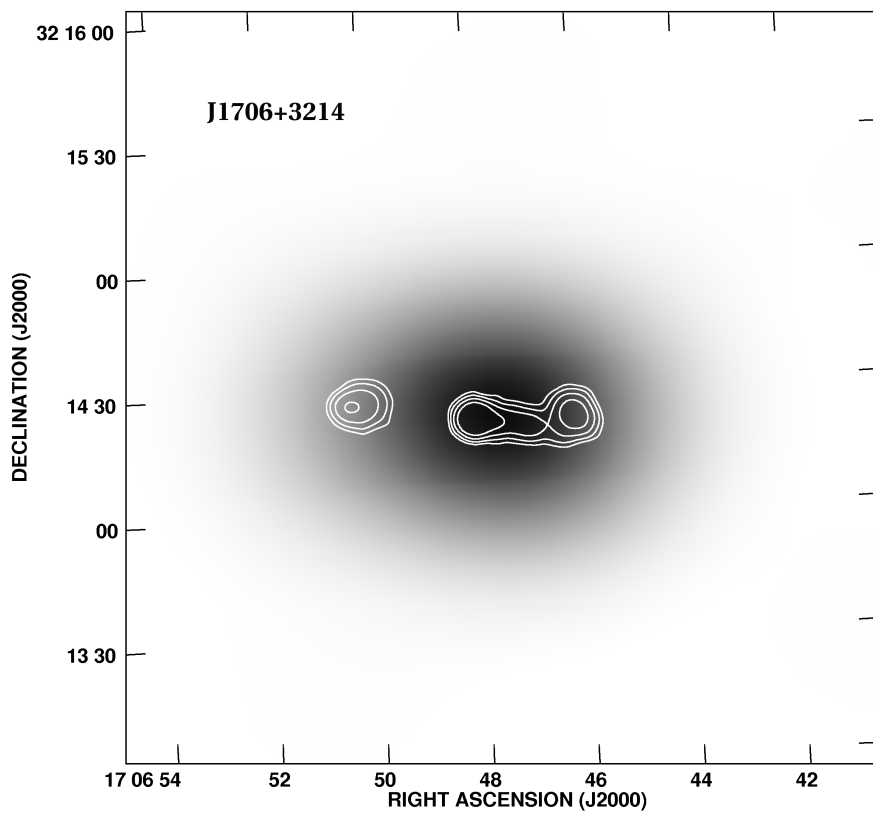
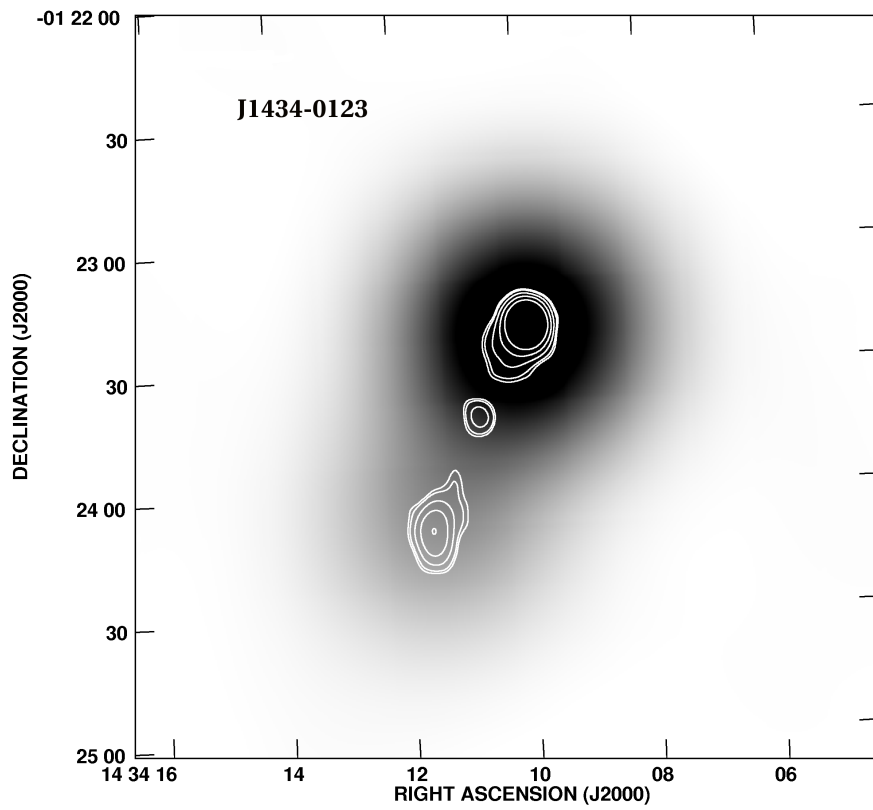


Fig. 4. The same as in Fig.2 but for J1434-0123 and J1706+3214

Table 3
3CRR sample of FR II-type sources with $z > 0.5$ and $\delta > 30^\circ$

Source	z	Id.	D [kpc]	R_T	ϕ [$^\circ$]	$\log P_{lf}$	$\log P_{1400}$	$\log P_{4850}$
(1)	(2)	(3)	(4)	(5)	(6)	(7)	(8)	(9)
3C6.1	0.8404	G	199	2.7	70	27.706 ^a	26.938	26.494
3C13	1.351	G	237	3.0	70	28.261 ^a	27.259	26.682
3C22	0.937	Q	190	3.0	70	27.780 ^a	26.920	26.403
3C34	0.689	G	341	4.3	90	27.656 ^a	26.474	25.815
3C41	0.794	G	175	2.4	70	27.404 ^b	26.851	26.491
3C54	0.8284	G	401	3.9	70	27.670 ^a	26.644	26.168
3C65	1.174	G	142	2.3	70	28.077 ^b	27.296	26.761
3C68.1	1.238	Q	386	2.4	50	27.967 ^b	27.239	26.767
3C68.2	1.575	G	191	2.3	70	28.290 ^b	27.259	26.548
3C169.1	0.633	G	315	2.7	70	27.287 ^a	26.214	25.700
3C184	0.99	G	35	4.0	70	27.832 ^a	27.017	26.514
3C196	0.871	Q	39	1.5	30	28.522 ^a	27.605	27.117
3C204	1.112	Q	257	3.4	70	28.032 ^a	26.857	26.267
3C205	1.534	Q	134	4.2	70	28.329 ^a	27.469	26.903
3C217	0.898	G	86	4.0	70	27.796 ^a	26.853	26.318
3C220.1	0.610	G	86	4.0	70	27.541 ^a	26.469	25.875
3C220.3	0.685	G	52	3.0	70	27.425 ^b	26.710	26.045
3C239	1.786	G	96	1.4	70	28.483 ^b	27.541	26.914
3C247	0.749	G	95	2.4	70	27.350 ^b	26.746	26.284
3C254	0.734	Q	96	2.0	50	27.974 ^a	26.791	26.198
3C263	0.6563	Q	307	2.7	50	27.616 ^a	26.634	26.182
3C263.1	0.824	G	41	1.7	70	27.696 ^b	26.911	26.369
3C265	0.8108	G	587	3.9	70	27.775 ^b	26.859	26.310
3C266	1.275	G	36	2.4	70	27.981 ^b	27.137	26.509
3C268.4	1.400	Q	83	2.8	50	28.123 ^a	27.273	26.774
3C270.1	1.519	Q	102	1.3	50	28.314 ^a	27.478	26.917
3C272	0.944	G	461	3.3	70	27.417 ^b	26.708	26.135
3C280	0.996	G	113	1.5	70	27.990 ^b	27.288	26.829
3C280.1	1.659	Q	169	4.0	70	28.267 ^a	27.343	26.771
3C289	0.967	G	81	1.3	70	27.686 ^b	26.966	26.430
3C292	0.71	G	960	4.2	90	27.406 ^b	26.547	26.075
3C294	1.779	G	135	1.9	70	28.413 ^b	27.431	26.840
3C322	1.681	G	283	2.5	70	28.171 ^b	27.485	26.954
3C324	1.207	G	85	1.8	70	27.999 ^b	27.257	26.712
3C325	0.860	G	122	2.2	70	27.657 ^b	27.011	26.481
3C330	0.549	G	395	5.4	90	27.432 ^b	26.771	26.334
3C337	0.635	G	295	2.5	70	27.522 ^a	26.599	26.125
3C352	0.8057	G	75	2.3	70	27.695 ^a	26.699	26.108
3C427.1	0.572	G	153	2.2	70	27.437 ^b	26.634	26.071
3C437	1.48	G	316	3.9	70	28.086 ^b	27.481	27.030
3C441	0.707	G	236	2.5	70	27.395 ^b	26.636	26.166
3C470	1.653	G	205	4.0	70	28.269 ^a	27.444	26.952

Table 4

Age and physical parameters of the sources in Sample 1

IAU name	t	α_{inj}	$\log Q_{jet}$	$\log \rho_0$	$\log p_h$	$\log U_c$	B_{eq}	v_h/c
(1)	[Myr] (2)	(3)	[W] (4)	[kg/m ³] (5)	[N/m ²] (6)	[J] (7)	[nT] (8)	(9)
J0037+0027	59.0	0.506	38.474	-23.311	-12.13	53.00	0.16	0.047
B0654+482	57.0	0.555	38.296	-22.741	-11.68	52.92	0.33	0.024
J0750+656	39.0	0.507	38.563	-23.670	-12.20	53.02	0.18	0.057
B0821+695	135.0	0.645	38.710	-22.968	-12.45	53.84	0.17	0.027
B0854+399	69.0	0.522	38.362	-22.992	-12.04	53.24	0.29	0.023
B1058+368	57.0	0.545	38.384	-22.741	-11.66	52.98	0.32	0.027
J1130-1320	100.0	0.537	39.005	-22.431	-11.71	53.90	0.33	0.028
B1602+376	47.0	0.524	38.621	-23.648	-12.35	53.35	0.22	0.041
B1636+418	38.0	0.526	38.367	-23.229	-11.82	52.83	0.29	0.037
B1834+620	75.0	0.533	38.455	-22.688	-11.80	53.18	0.28	0.026
J1951+706	73.0	0.525	38.061	-22.921	-12.02	52.73	0.25	0.025
J2234-0224	(91.0)		(38.1)	(-22.55)				0.019

Table 5

Age and physical parameters of the sources in Sample 2

IAU name	t	α_{inj}	$\log Q_{jet}$	$\log \rho_0$	$\log p_h$	$\log U_c$	B_{eq}	v_h/c
(1)	[Myr] (2)	(3)	(4)	[kg/m ³] (5)	[N/m ²] (6)	[J] (7)	[nT] (8)	(9)
J0245+0108	18.5	0.603	39.295	-22.153	-10.30	53.45	1.74	0.038
J0809+2912	7.5	0.496	39.715	-24.555	-11.65	53.59	0.41	0.233
J0839+2928	21.5	0.535	38.655	-23.031	-11.44	52.93	0.62	0.031
J0857+0906	14.6	0.564	39.111	-22.629	-10.48	53.08	1.13	0.054
J0947+5154	50.5	0.624	38.508	-21.616	-10.62	53.06	1.12	0.015
J0952+0628	23.0	0.554	38.806	-22.453	-10.75	52.98	0.89	0.037
B1011+365	18.1	0.542	38.752	-22.686	-10.76	52.94	1.00	0.036
J1030+5310	28.0	0.548	38.605	-23.408	-11.77	53.05	0.38	0.042
B1108+359	23.3	0.655	39.560	-21.913	-10.22	53.90	2.18	0.031
B1109+437	4.3	0.544	40.028	-23.238	-10.04	53.47	1.87	0.175
J1130+3628	29.5	0.536	38.180	-22.898	-11.39	52.53	0.47	0.027
J1550+3652	6.6	0.511	39.340	-24.327	-11.42	53.16	0.53	0.160
J1706+3214	36.6	0.572	38.460	-22.340	-11.00	52.90	0.72	0.022
B1723+510	23.5	0.661	39.676	-21.881	-10.09	53.92	1.98	0.041
J2345-0936	29.6	0.564	38.797	-22.308	-10.82	53.23	1.05	0.024
B2352+796	16.0	0.578	39.747	-22.155	-10.08	53.74	1.83	0.058

Table 6

Age and physical parameters of the sources in Sample 3. The age solution for the sources which name is followed by the asterisk is provided by J. Machalski (unpublished).

IAU name	t	α_{inj}	$\log Q_{jet}$	$\log \rho_0$	$\log p_h$	$\log U_c$	B_{eq}	v_h/c
(1)	[Myr]	(3)	[W]	[kg/m ³]	[N/m ²]	[J]	[nT]	(9)
3C6.1	5.12	0.564	39.298	-22.891	-10.08	53.03	2.75	0.057
3C13	5.87	0.583	39.606	-22.549	-9.81	53.35	3.41	0.060
3C22	4.68	0.559	39.316	-22.799	-9.92	52.96	3.03	0.060
3C34	24.0	0.630	39.012	-21.434	-9.86	53.22	2.56	0.018
3C41	1.52	0.534	39.580	-24.250	-10.34	52.85	2.21	0.182
3C54*	15.2	0.562	39.141	-22.280	-10.26	53.17	1.64	0.039
3C65	3.40	0.588	39.604	-22.881	-9.74	53.23	4.65	0.065
3C68.1*	7.94	0.564	39.784	-23.053	-10.43	53.66	1.70	0.089
3C68.2	4.35	0.771	40.209	-22.406	-9.41	53.94	6.97	0.076
3C169.1	24.7	0.575	38.611	-22.230	-10.68	53.02	1.37	0.019
3C184	0.37	0.577	39.471	-23.395	-8.46	52.01	12.83	0.142
3C196	0.60	0.579	40.042	-23.374	-8.91	52.82	10.14	0.188
3C204	11.6	0.625	39.350	-21.969	-9.76	53.36	3.28	0.035
3C205	1.45	0.584	39.949	-22.840	-8.98	52.95	6.76	0.143
3C217	1.87	0.588	39.301	-22.481	-8.97	52.41	7.08	0.068
3C220.1	11.0	0.610	38.900	-21.653	-9.53	52.78	3.74	0.024
3C220.3	1.92	0.580	38.955	-22.345	-8.97	52.21	9.01	0.040
3C239*	2.90	0.673	39.903	-22.904	-9.68	53.60	7.61	0.052
3C247*	1.70	0.547	39.182	-23.182	-9.88	52.50	3.77	0.087
3C254	5.60	0.627	39.172	-22.240	-9.60	52.98	5.18	0.031
3C263	12.8	0.557	39.126	-22.584	-10.44	53.15	1.53	0.044
3C263.1*	1.30	0.600	39.133	-23.110	-9.40	52.43	8.83	0.050
3C265*	27.0	0.609	39.415	-21.905	-10.25	53.72	1.66	0.034
3C266*	0.86	0.639	39.462	-22.674	-8.64	52.48	16.12	0.065
3C268.4	0.95	0.574	39.809	-23.280	-9.15	52.70	6.56	0.159
3C270.1*	2.35	0.568	39.708	-23.458	-10.07	53.26	4.30	0.079
3C272*	19.0	0.557	39.132	-22.484	-10.57	53.37	1.32	0.038
3C280*	2.60	0.560	39.520	-23.578	-10.23	53.16	3.76	0.068
3C280.1	2.50	0.574	39.795	-22.635	-9.23	53.03	5.24	0.100
3C289*	3.60	0.571	39.080	-23.296	-10.30	52.88	3.92	0.035
3C292*	38.0	0.566	39.180	-22.266	-10.86	53.60	0.81	0.035
3C294*	3.65	0.683	39.950	-22.611	-9.54	53.67	6.95	0.058
3C322*	4.00	0.557	39.908	-23.310	-10.16	53.58	2.66	0.111
3C324*	2.20	0.584	39.471	-23.117	-9.71	52.98	5.91	0.061
3C325*	2.90	0.566	39.320	-23.197	-9.95	52.89	3.77	0.066
3C330*	6.60	0.543	39.404	-22.699	-9.98	52.93	1.82	0.084
3C337	11.3	0.553	38.999	-22.853	-10.64	53.10	1.53	0.039
3C352	2.96	0.595	38.986	-22.631	-9.55	52.53	5.78	0.038
3C427.1*	9.10	0.592	38.903	-22.498	-10.18	52.98	2.91	0.026
3C437*	2.42	0.546	40.113	-23.405	-9.80	53.37	2.78	0.205
3C441*	10.0	0.556	38.984	-22.764	-10.45	53.05	1.91	0.037
3C470	1.97	0.550	39.973	-23.063	-9.41	53.10	4.25	0.155

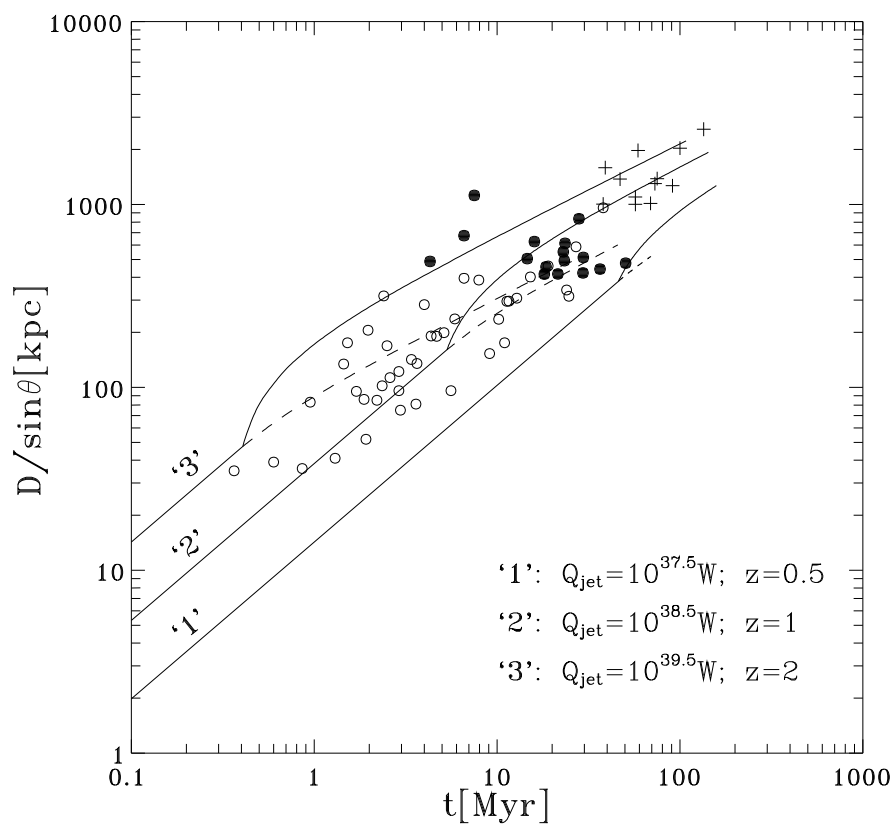


Fig. 5. D vs t diagrams for three sets of the jet power and redshift. The solid lines indicate the model predictions in the frame of Scenario A, the dashed lines – in Scenario B. The sources from the Samples 1, 2, and 3 are plotted with the crosses, full dots, and open circles, respectively.

Table 7: Observational and dynamical parameters of seven FR II-type radio galaxies with $0.1 \lesssim z \lesssim 0.2$, for which their dynamical age determined with the DYNAGE is $12 \text{ Myr} < t < 36 \text{ Myr}$.

Name	z	D [kpc]	$\log P_{1400}$ [W/(Hz·sr)]	t [Myr]	$\log Q_{\text{jet}}$ [W]	$\log \rho_0$ [kg/m ³]
3C332	0.1515	229	25.07	36	37.45	-22.60
3C349	0.205	287	25.46	29	37.91	-22.44
3C357	0.1664	296	25.20	24	37.77	-22.96
3C381	0.1605	199	25.29	25	37.66	-22.76
B0908+376	0.1047	229	24.12	20	36.50	-23.59
B1130+339	0.2227	99	24.98	12	37.38	-23.01
B1457+292	0.146	172	24.15	28	36.80	-23.99

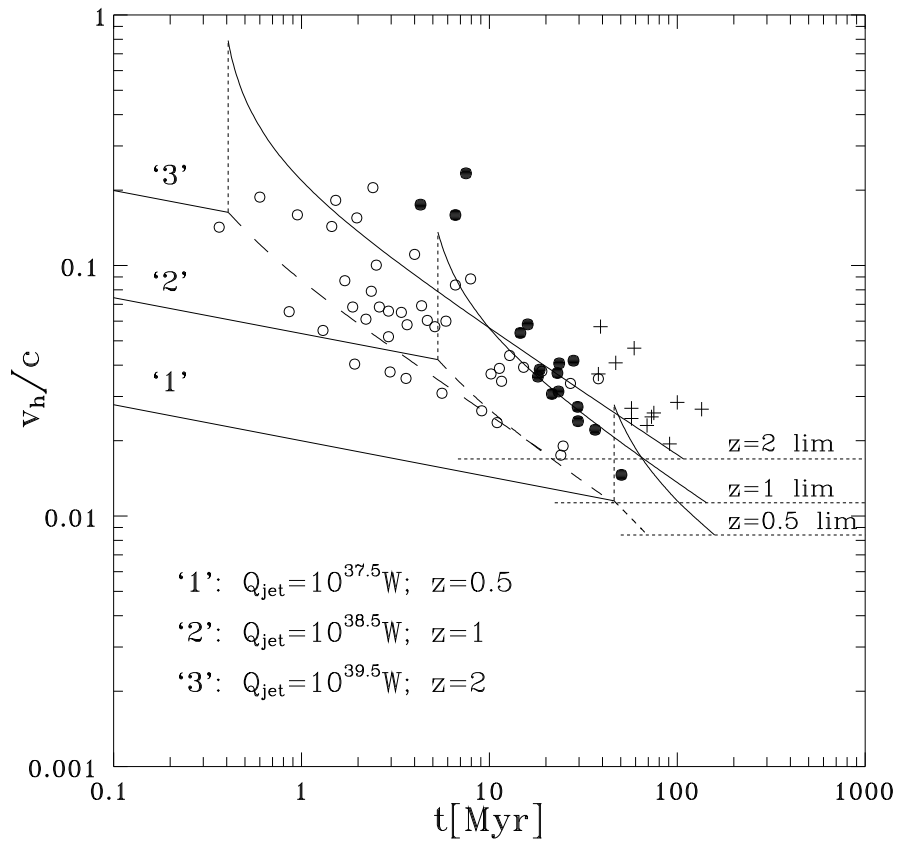


Fig. 6. v_h/c vs t diagrams for the same sets of the model parameters as in Fig. 5. The three horizontal dotted lines indicate the lower limits for the expansion velocity determined by the sound speed at a given redshift.

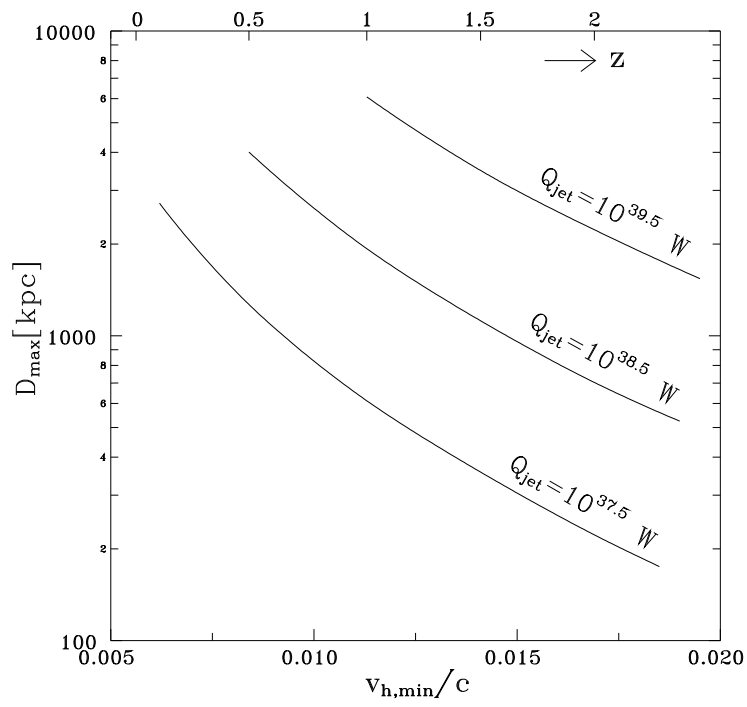


Fig. 7. D_{\max} vs v_{\min}/c diagrams for three values of the jet power.

Table 8

The newly discovered FR II-type sources with $1 < z < 2$ and $D > 400$ kpc in Sample 2 and their observational parameters.

IAU name	RA (J2000) [h m s]	DEC (J2000) [° ' "]	LAS [arcsec]	$S_{1400\text{MHz}}$ [mJy]
J0245+0108	02 45 34.07	+01 08 13.7	53.4	327
J0809+2015	08 09 20.81	+20 15 38.6	56.3	84.8
J0809+2912	08 09 06.22	+29 12 35.5	129	304
J0812+3031	08 12 40.08	+30 31 09.4	146	24.5
J0819+0549	08 19 41.13	+05 49 42.7	115	27.4
J0839+2928	08 39 51.75	+29 28 18.2	50.5	113
J0842+2147	08 42 39.96	+21 47 10.4	130	49.2
J0857+0906	08 57 48.57	+09 06 48.1	59.1	130
J0902+5707	09 02 07.20	+57 07 37.9	101	29.8
J0906+0832	09 06 49.99	+08 32 55.9	79.8	78.7
J0947+5154	09 47 40.01	+51 54 56.8	58.6	111
J0952+0628	09 52 28.46	+06 28 10.5	65.0	127
J1030+5310	10 30 50.91	+53 10 28.6	100	56.4
J1039+0714	10 39 36.67	+07 14 27.4	58.6	24.7
J1130+3628	11 30 26.18	+36 28 36.9	51.6	45.2
J1207-0244	12 07 08.02	-02 44 44.2	54.6	62.1
J1434-0123	14 34 10.77	-01 23 41.7	60.6	119
J1550+3652	15 50 02.01	+36 52 16.8	80.4	47.4
J1706+3214	17 06 48.07	+32 14 22.9	54.2	125
J2345-0936	23 45 40.45	-09 36 10.2	60.9	223